

A Generalized Open Quantum System Approach for the Electron Paramagnetic Resonance of Magnetic Atoms

Gal Shavit,¹ Baruch Horovitz,² and Moshe Goldstein¹

¹*Raymond and Beverly Sackler School of Physics and Astronomy, Tel Aviv University, Tel Aviv 6997801, Israel*

²*Department of Physics, Ben-Gurion University of the Negev, Beer Sheva 84105, Israel*

A recent experimental breakthrough allowed to probe electronic parametric resonance of a single magnetic atom in a scanning tunneling microscopy (STM) setup. The results present intriguing features, such as an asymmetric lineshape and unusually large ratio of the decoherence and decay rates, which defy standard approaches using the conventional Bloch equations. To address these issues we employ novel generalized Bloch equations, together with proper microscopic modeling of the magnetic adatom, and show how all the experimental features can be naturally accounted for. The proposed approach may also be useful in treating any future similar experiments, as well as next generation hybrid quantum devices.

I. INTRODUCTION

Electron paramagnetic resonance (EPR) experiments have been a powerful tool in studying the properties of different paramagnetic materials by probing the spin of unpaired electrons for several decades¹. Recently, the possibility of single spin resolution in EPR detection has been realized by utilizing STM to measure the tunneling conductance through a magnetic impurity²⁻⁷, where a spin-polarized STM tip is used both as the EPR pump and probe. A different type of EPR-STM phenomena was realized by using a non-polarized tip^{8,9}.

Focusing here on experiments with polarized tips, the results of these experiments pose several difficulties. First, a conspicuous asymmetry in the resonance lineshape, with the signal even dropping below its asymptotic value; this was previously attributed to phenomenological Fano interferences^{4,10}. Second, a T_1 relaxation time which is about three orders of magnitude longer than the decoherence time T_2 . As we will show, these features (and others to be detailed below) can naturally be explained as intrinsic effects provided we: (a) go beyond the traditional Bloch equation employed in these works, and use a new generalized quantum master equation; (b) account for the fact that the two level system addressed by the EPR excitation is a part of a more complex energy manifold of the adatom; (c) derive relaxation rates from the spin-electrode couplings.

The paper is organized as follows. In Sec. II we present the theoretical model for the experimental system, as well as its mapping to an effective open quantum two-level system (TLS). We then show how a measurement of the tunneling current reveals the steady state polarization of the TLS in Sec. III. The flaws in treating the system using traditional approaches are pointed out in Sec. IV, leading to an introduction of our novel generalized approach in Sec. V. After showing that our proposed treatment can account for some of the experimental observations, in Sec. VI we consider the higher voltage regimes, where higher energy levels play a role, and show that our approach captures the unique features observed in this regime. We summarize our findings in Sec. VII. We

give additional technical details regarding the derivation of our generalized approach in Appendix A, and expand on the calculation of relaxation and decoherence rates in Appendix B.

II. MODEL

To make the discussion concrete we concentrate on the system studied in Ref.³ (see Fig. 1). There, single iron atoms were placed on a monolayer magnesium oxide (MgO) film, isolating the atoms from a bulk silver substrate. A spin-polarized STM tip was positioned above the iron adatom, with the direction of its polarization determined by the applied magnetic field, which is at an angle ψ to the axis perpendicular to the MgO plane, whose value was close to 90° (field nearly parallel to the substrate). The magnetic atom placed on the substrate (assumed to be in the d^6 electronic configuration in the lowest Hund's term, with $L = S = 2$) is well described by the ligand-field Hamiltonian¹¹

$$H_{\text{lf}} = DL_z^2 + EL_z^4 + F_0(L_+^4 + L_-^4) + \lambda \vec{L} \cdot \vec{S} + \mu_B (\vec{L} + 2\vec{S}) \cdot \vec{B}, \quad (1)$$

with the applied magnetic field \vec{B} and the Bohr magneton μ_B . The values used for the parameters in H_{lf} are given in Table I. This Hamiltonian includes all terms allowed by the four-fold symmetry of the Fe bound to the MgO layer. A finite magnetic field component in the direction perpendicular to the MgO substrate acts as a Zeeman field, splitting the lowest energy state of the atom into an effective TLS, polarized in its spin component, and isolated from the rest of the spectrum by a gap of roughly ~ 14 meV³. A dc voltage $V_{\text{dc}} = 5$ mV was set between the tip and the substrate, allowing tunneling of electrons between the tip and the bulk substrate through the adatom. Additionally, an rf voltage was introduced, driving coherent transitions of the TLS.

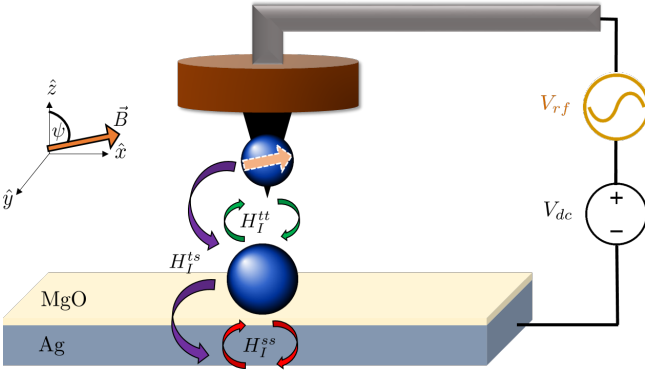


FIG. 1. Experimental setup of the EPR-STM experiment^{3,4}. The iron adatom is placed on an MgO substrate below an STM tip. Applying an appropriate magnetic field \vec{B} effectively turns the atom into a TLS in the working dc voltage regime and polarizes the STM tip in the field direction. An additional rf voltage is applied between the tip and the substrate to measure the electron paramagnetic resonance in the atom. Also shown is a schematic depiction of the exchange interaction processes between the adatom and the bath electrons. The strength of the exchange interaction for electrons hopping from tip to the adatom and back (green) is J_t , for electrons hopping from the substrate and back (red) is J_s , and for electrons tunneling from the tip to the substrate (or the other way around) through the adatom (purple) is $\sqrt{J_t J_s}$.

| Parameter | Approximate value |
|-----------|-------------------|
| D | -433 meV |
| E | 0 meV |
| F_0 | 2.19 meV |
| λ | -12.6 meV |

TABLE I. Approximate values for the free parameters in the ligand-field Hamiltonian (Eq. (1)), see Supplementary Material for³.

Projecting (1) into its two lowest levels and including the periodic drive and the coupling of the atom to the tip and substrate electrons, one finds the total Hamiltonian

$$H = H_S + H_D + H_I + H_B, \quad (2)$$

with H_S , H_D , H_I and H_B representing the system, periodic driving, interaction of the TLS with the electronic bath (phononic dissipation is neglected as a result of the low temperature, $T \approx 0.6$ K) and bath Hamiltonians respectively, and are given by

$$H_S = -\frac{1}{2}\hbar\omega_0\sigma_z, \quad (3a)$$

$$H_D = \hbar\Omega \cos(\omega_d t) \sigma_x, \quad (3b)$$

$$H_I = H_I^{ss} + H_I^{tt} + H_I^{ts}, \quad (3c)$$

$$H_B = \sum_{k,\sigma,\ell} \left(\epsilon_{k\sigma\ell} c_{k\sigma\ell}^\dagger c_{k\sigma\ell} + T_0 c_{k\sigma\ell}^\dagger c_{k\sigma\bar{\ell}} \right), \quad (3d)$$

where $\vec{\sigma}$ are the Pauli matrices in the TLS subspace, $\hbar\omega_0$ is the two-level energy separation, $\Omega \propto V_{\text{rf}}$ is the driving amplitude, $\omega_d \equiv \omega_0 + \delta\omega$ is the driving frequency (typically $\Omega = 1 - 20$ MHz, $\omega_0, \omega_d \sim 25$ GHz). The driving Ω and detuning $\delta\omega$ combine to give the generalized Rabi frequency $\omega \equiv \sqrt{\Omega^2 + \delta\omega^2}$, T_0 is the tip-substrate tunneling amplitude, and $c_{k\sigma\ell}$ is an electronic annihilation operator with momentum k and spin σ in reservoir ℓ (either the tip or the substrate, with $\bar{\ell}$ the reservoir opposing ℓ). The three different components of the interaction Hamiltonian H_I describe different hopping processes of electrons: tip-atom-tip (tt), substrate-atom-substrate (ss), and tip-atom-substrate (ts), see Fig. 1. They are of the form

$$H_I^{\ell\ell'} = \sqrt{J_\ell J_{\ell'}} \vec{S} \cdot \vec{S}_{\ell\ell'}, \quad (4)$$

with $\vec{S}_{\ell\ell'} = \sum_{k,k'} \left(c_{k\sigma\ell}^\dagger \vec{\sigma}_{\sigma\sigma'} c_{k'\sigma'\ell'} + \text{h.c.} \right)$. \vec{S} is the *physical* spin operator of the magnetic atom, while σ , whenever next to c, c^\dagger operators, operates within the spin space of the tunneling electrons.

A. Mapping the interaction Hamiltonian into an open TLS

The Hamiltonian Eq. (1) can be diagonalized in the 5×5 Hilbert space spanning the different orbital momentum and spin states. We shall henceforth focus on the two lowest energy levels of H_{lf} , denoted by $|0\rangle$ and $|1\rangle$. Any operator \hat{O} can be projected onto the subspace spanned by the TLS,

$$\hat{O} = \frac{1}{2}\sigma_x (O_{10} + O_{01}) + \frac{i}{2}\sigma_y (O_{10} - O_{01}) + \frac{1}{2}\sigma_z (O_{00} + O_{11}) + \frac{1}{2}(O_{00} - O_{11}), \quad (5)$$

with the matrix elements $O_{ij} \equiv \langle i | \hat{O} | j \rangle$. In this manner, we can map all spin operators in the two-level subspace using the general notation

$$\begin{pmatrix} S_x \\ S_y \\ S_z \end{pmatrix} = \begin{pmatrix} \alpha_{xx} & \alpha_{xy} & \alpha_{xz} \\ \alpha_{yx} & \alpha_{yy} & \alpha_{yz} \\ \alpha_{zx} & \alpha_{zy} & \alpha_{zz} \end{pmatrix} \begin{pmatrix} \sigma_x \\ \sigma_y \\ \sigma_z \end{pmatrix}. \quad (6)$$

Using the parameters in Table I, we evaluate the spin projection matrix,

$$\begin{pmatrix} \alpha_{xx} & \alpha_{xy} & \alpha_{xz} \\ \alpha_{yx} & \alpha_{yy} & \alpha_{yz} \\ \alpha_{zx} & \alpha_{zy} & \alpha_{zz} \end{pmatrix} \approx -2 \cdot 10^{-4} \begin{pmatrix} 2.4 & 0 & -1 \\ 0 & 2.4 & 0 \\ 7.1 & 0 & 10^4 \end{pmatrix}. \quad (7)$$

Importantly, α_{zz} is by far the most dominant matrix element, and we find the approximation $\alpha_{xx} \approx \alpha_{yy} \equiv \alpha_\perp$ well justified.

The quantization axis of the spin in the interaction Hamiltonian (4), the \hat{z} axis, is directed along the “lab”

\hat{z} direction, normal to the substrate (which is also the easy axis of the adatom deposited on the MgO layer). We perform a rotation on the electronic operators such that the new spin axis lies in the direction of the STM tip spin-polarization (similarly to¹²)

$$c_{k\uparrow\ell} \rightarrow \cos \frac{\psi}{2} c_{k\uparrow\ell} - \sin \frac{\psi}{2} c_{k\downarrow\ell}, \quad (8a)$$

$$c_{k\downarrow\ell} \rightarrow \sin \frac{\psi}{2} c_{k\uparrow\ell} + \cos \frac{\psi}{2} c_{k\downarrow\ell}. \quad (8b)$$

After this rotation, we write the interaction Hamiltonian as

$$H_I^{\ell\ell'} \equiv \sqrt{J_\ell J_{\ell'}} \left(\sigma_+ \hat{\Sigma}_+ + \sigma_- \hat{\Sigma}_- + \sigma_z \hat{\Sigma}_z \right), \quad (9)$$

with the electronic operators $\hat{\Sigma}_i$,

$$\begin{aligned} \hat{\Sigma}_- = & \left(\alpha_{zx} \cos \psi + \frac{\alpha_\perp}{2} \sin \psi \right) \times \\ & \sum_{k,k',\sigma} \sigma \left(c_{k\sigma\ell}^\dagger c_{k'\sigma\ell'} + c_{k'\sigma\ell'}^\dagger c_{k\sigma\ell} \right) \\ & + \left(\frac{\alpha_\perp}{2} (\cos \psi + 1) - \alpha_{zx} \sin \psi \right) \times \\ & \sum_{k,k'} \left(c_{k\downarrow\ell}^\dagger c_{k'\uparrow\ell'} + c_{k'\downarrow\ell'}^\dagger c_{k\uparrow\ell} \right) \\ & + \left(\frac{\alpha_\perp}{2} (\cos \psi - 1) - \alpha_{zx} \sin \psi \right) \\ & \sum_{k,k'} \left(c_{k\uparrow\ell}^\dagger c_{k'\downarrow\ell'} + c_{k'\uparrow\ell'}^\dagger c_{k\downarrow\ell} \right), \end{aligned} \quad (10)$$

$$\begin{aligned} \hat{\Sigma}_z = & \left(\alpha_{zz} \cos \psi + \frac{1}{2} \alpha_{xz} \sin \psi \right) \sum_{k,k',\sigma} \sigma c_{k\sigma\ell}^\dagger c_{k'\sigma\ell'} \\ & + \left(\frac{1}{2} \alpha_{xz} \cos \psi - \alpha_{zz} \sin \psi \right) \sum_{k,k',\sigma} c_{k\sigma\ell}^\dagger c_{k'\bar{\sigma}\ell'} + \text{h.c.}, \end{aligned} \quad (11)$$

and $\hat{\Sigma}_+ = (\hat{\Sigma}_-)^\dagger$.

III. RELATING THE TUNNELING CURRENT TO THE TLS POLARIZATION

We consider the tunneling current due to interactions with the reservoirs, following mainly the treatment in¹². The labels ℓ, ℓ' refer here to the tip and substrate, respectively. The current operator may be determined by examining the change in total charge over time in one of the leads,

$$I(t) = ie \left[\sum_{k,\sigma} c_{k\sigma t}^\dagger c_{k\sigma t}, H \right] = ie (C - C^\dagger), \quad (12)$$

with

$$C \equiv T_0 \sum_{k,k',\sigma} c_{k\sigma t}^\dagger c_{k'\sigma s} e^{ieVt} + J_{ts} \sum_{k,k',\sigma,\sigma'} c_{k\sigma t}^\dagger \vec{\sigma}_{\sigma\sigma'} \cdot \vec{S}_{k'\sigma's} e^{ieVt}, \quad (13)$$

and $J_{ts} = \sqrt{J_t J_s}$. We can expand the average of the current operator to lowest (first) nonvanishing order in the tunneling Hamiltonian, using the relation $\langle \hat{O}(t) \rangle = -i \int_{-\infty}^t dt' \langle [\hat{O}(t), H_T(t')] \rangle_0$, where the average inside the integral is taken in the zero tunneling state. We find

$$\langle I(t) \rangle = e \int_{-\infty}^t dt' \langle [C(t'), C^\dagger(t)] \rangle_0 + \text{c.c.} \quad (14)$$

The expression in Eq. (14) can be divided into three individual contributions, proportional, respectively, to T_0^2 , J_{ts}^2 and $T_0 J_{ts}$. The first contribution corresponds to background current, which is unaffected by the adatom spin. The second term will be significantly weaker compared to the last one due to the fact that typically $\frac{J_{ts}}{T_0} \sim 0.1$ (the ratio between the spin exchange energy and the spin-independent tunneling amplitude¹²). Hence, we shall focus on the $T_0 J_{ts}$ term, which we denote by $I_{T_0 J}$. Neglecting any scattering between the different momentum/spin channels in the $\langle \dots \rangle_0$ average, and using the Fermi-Dirac distribution $f(\epsilon_k)$, we find

$$\begin{aligned} \langle I_{T_0 J}(t) \rangle = & e T_0 J_{ts} \sum_{k,k',\sigma} \sigma_{\sigma\sigma}^z \int_{-\infty}^t dt' e^{i[eV + \epsilon_{k\sigma} - \epsilon_{k'\sigma'}](t'-t)} \times \\ & [f_{\ell'\sigma}(k) (1 - f_{\ell\sigma}(k')) \langle S^z(t') \rangle \\ & - f_{\ell\sigma}(k) (1 - f_{\ell'\sigma}(k')) \langle S^z(t) \rangle] + \text{c.c.} \end{aligned} \quad (15)$$

We set the local densities of states $\nu_{\ell'\sigma} = \frac{\nu_t}{2} (1 + \sigma p)$, $\nu_{\ell\sigma} = \frac{\nu_s}{2}$, which is possible since we choose here the \hat{z} direction to be the tip spin-polarization axis, denoted as \hat{p} in the following. Moving to a summation over energies instead of momenta, and taking the long-time limit such that $\langle S_{\hat{p}} \rangle$ reaches its steady state,

$$\begin{aligned} \langle I_{T_0 J} \rangle = & e T_0 J_{ts} \frac{\nu_s \nu_t}{2} p \langle S_{\hat{p}} \rangle \int_{-\infty}^{\infty} d\tau e^{i(eV + \epsilon - \epsilon')\tau} \times \\ & \int_{-\infty}^{\infty} d\epsilon' \int_{-\infty}^{\infty} d\epsilon \times \\ & [f(\epsilon) (1 - f(\epsilon')) - f(\epsilon') (1 - f(\epsilon))] + \text{c.c.} \end{aligned} \quad (16)$$

Performing the integration over τ will result in a delta function. Assuming $eV \gg k_B T$ (in the experiment $eV = 5\text{--}60$ meV and $k_B T \approx 50$ μeV), we find

$$\langle I_{T_0 J} \rangle \approx \pi e^2 V T_0 J_{ts} \nu_s \nu_t p \langle S_{\hat{p}} \rangle, \quad (17)$$

i.e., the spin-dependent contribution to the current is proportional to the steady-state spin polarization of the intermediary adatom in the direction of the tip polarization.

The physical spin polarization can be expressed in terms of TLS expectation values,

$$\langle S_{\hat{p}} \rangle = (\alpha_{xz} \sin \psi + \alpha_{zz} \cos \psi) \langle \sigma_z \rangle + (\alpha_{\perp} \sin \psi + \alpha_{zx} \cos \psi) \langle \sigma_x \rangle. \quad (18)$$

Since α_{zz} overwhelmingly dominates the other matrix elements, and taking into account $\psi \approx 80^\circ - 88^\circ$ in these experiments, we conclude that

$$\langle I_{T_0 J} \rangle \propto \alpha_{zz} \langle \sigma_z \rangle, \quad (19)$$

so that the tunneling current is a direct measurement of the TLS polarization. Sweeping the driving frequency and measuring the change in current (compared to the non-driven $\Omega = 0$ case), resonant lineshapes may be observed, with the resonant frequency corresponding to the energy separation of the TLS.

IV. FAILURE OF STANDARD BLOCH EQUATIONS

Ref.³ analyzed the TLS dynamics using the Bloch equations [Supplementary Material for³, Eq. (S1)]. Writing the adatom density matrix in the form $\rho \equiv \frac{1}{2} + (n - \frac{1}{2})\sigma_z + \alpha^*\sigma_- + \alpha\sigma_+$, the equations may be written in the frame rotating with ω_d as

$$\frac{d}{dt}n = -n(\Gamma_{\downarrow} + \Gamma_{\uparrow}) + \Gamma_{\uparrow} - i\Omega \frac{\alpha - \alpha^*}{2}, \quad (20a)$$

$$\frac{d}{dt}\alpha = -\alpha \left(\frac{\Gamma_{\downarrow} + \Gamma_{\uparrow}}{2} + 2\Gamma^z + i\delta\omega \right) - i\Omega \left(n - \frac{1}{2} \right) \quad (20b)$$

with Γ_{\downarrow} , Γ_{\uparrow} and Γ^z the relaxation, excitation, and pure dephasing rates, which are given by ($a = -1, 1$ corresponding to \downarrow, \uparrow , respectively)

$$\Gamma_a \equiv \frac{1}{2} \text{Re} \left\{ \int_0^\infty d\tau e^{-ia\omega_d\tau} \text{Tr}_B \left\{ \rho_B \hat{\Sigma}_a(\tau) \hat{\Sigma}_{-a}(0) \right\} \right\} \quad (21)$$

$$\Gamma^z \equiv \frac{1}{2} \text{Re} \left\{ \int_0^\infty d\tau \text{Tr}_B \left\{ \rho_B \hat{\Sigma}_z(\tau) \hat{\Sigma}_z(0) \right\} \right\}, \quad (22)$$

where $\text{Tr}_B \{ \cdot \}$ is a trace over the bath degrees of freedom (the reservoir electrons), and ρ_B is the bath density matrix. The commonly used decay times are then $\frac{1}{T_1} = \Gamma_{\downarrow} + \Gamma_{\uparrow}$ and $\frac{1}{T_2} = \frac{1}{2T_1} + 2\Gamma^z \equiv \tilde{\Gamma}$, where in the experiment Ref.³ $T_1 \sim 100 \mu\text{sec}$, $T_2 \sim 100 \text{nsec}$. Eqs. (20a)–(20b) are obtained by first deriving a master equation for the density matrix in the absence of driving, and then adding the drive “after the fact”, such that it does not impact the dissipative terms. In particular, it assumes relaxation towards the lab frame z axis, as if the drive were absent. As our more general treatment will show, this *lab frame approach*, common mainly in atomic physics^{13,14} and quantum optics¹⁵, neglects the difference between the values of the bath spectral functions

at frequencies $0, \pm\omega_d$ [Eqs. (21)–(22)], and their values at $\pm\omega, \pm\omega_d \pm \omega$, respectively. While one might expect these differences to be small for $\omega \ll T, V, \omega_d$, which is the case here, we will show below that the importance of some of these small differences is enhanced due to the non-equilibrium nature of the system.

Solving (20a)–(20b) for the steady state of the system and extracting $\langle \sigma_z \rangle = n - \frac{1}{2}$ results in

$$\langle \sigma_z^\infty \rangle_{\text{Bloch}} = \frac{(\Gamma_{\uparrow} - \Gamma_{\downarrow}) (\tilde{\Gamma}^2 + \delta\omega^2)}{(\Gamma_{\downarrow} + \Gamma_{\uparrow}) (\tilde{\Gamma}^2 + \delta\omega^2) + \tilde{\Gamma}\Omega^2}, \quad (23)$$

which is *even* in the detuning frequency $\delta\omega$, and thus cannot reproduce the distinct asymmetric shape observed in many experiments on these systems^{3–7}. The asymmetric lineshape was attributed to an extrinsic effect, namely the interplay between the precession of the tunnel conductance and the rf voltage (Supplementary Materials to Refs.^{4,16}). However, this phenomenological description does not contain a physical reason for neither the conductance oscillations nor for the asymmetric lineshape. Moreover, the unusually high value of the ratio T_1/T_2 found in these experiments still needs to be accounted for. Below we show that both phenomena are *intrinsic* to the system.

One common possible alternative approach which includes modifications to the dissipator stemming from the driving, may be obtained by diagonalizing $H_S + H_D$ in a frame rotating with the driving frequency ω_d , and only then calculating the dissipative dynamics, now with a modified system-bath interaction due to the driving. However, in order for the master equation to be of Lindblad form^{17,18}, this *rotating frame approach* requires an additional “secular approximation” with regards to the generalized Rabi frequency ω , i.e., that it is sufficiently greater than all the dissipative rates. This approximation is inadequate in the experiments discussed here, where $\omega T_2 \lesssim 1$.

V. GENERALIZED BLOCH EQUATIONS

We develop and solve a novel *generalized approach* by working in the rotating frame but avoiding the customary secular approximation¹⁹ with regards to the low Rabi frequency, while keeping the secular approximation only for the high frequencies ω_0, ω_d . Our approach then covers the entire crossover range between $\omega = 0$ (lab frame approach) and $\omega \gg \frac{1}{T_1}, \frac{1}{T_2}$ (rotating frame approach). Crucially, the generalized approach keeps the distinction between bath correlations calculated at frequencies $\pm\omega$ and those at 0 , while neglecting the distinction between correlations at $\pm\omega_d$ and $\pm\omega_d \pm \omega$. The latter distinction is negligible since for $\omega \ll \omega_d$, as we have explicitly checked. The distinction between frequencies $\pm\omega$ and 0 necessitates the introduction of Γ_{\pm}^z , which are similar to

Γ_z [Eq. (21)] but at frequencies $\pm\omega$,

$$\Gamma_{\pm}^z = \frac{1}{2} \text{Re} \left\{ \int_0^\infty d\tau e^{\pm i\omega\tau} \text{Tr}_B \left\{ \rho_B \hat{\Sigma}_z(\tau) \hat{\Sigma}_z(0) \right\} \right\}. \quad (24)$$

With this treatment, subtle changes in the bath spectral density from a frequency shift of order $\sim \omega$ may be taken into account, without any restrictions on the size of the decay rates themselves. As we subsequently show, in the EPR-STM experiments discussed in this work this fact is crucial to interpreting the measured results. The absence of perturbative assumptions regarding the Rabi frequency gives rise to an imbalance in the excitation and relaxation rates in the rotating frame [see Eq. (A9a)], translating to an asymmetry in the EPR lineshape, which was previously not accounted for.

The generalized approach thus results in a more complicated master equation (see Appendix A for the full derivation), where (20a) remains unchanged but (20b) is modified to

$$\begin{aligned} \frac{d}{dt} \alpha = & \left[\frac{d}{dt} \alpha \right]_{\text{Bloch}} - \frac{\Gamma_+^z - \Gamma_-^z}{2} \cos \beta \\ & + (\Gamma_+^z + \Gamma_-^z - 2\Gamma^z) \left[\left(n - \frac{1}{2} \right) \frac{\sin 2\beta}{2} - \alpha \cos^2 \beta \right], \end{aligned} \quad (25)$$

with $\tan \beta \equiv \frac{\delta\omega}{\Omega}$. It is sufficient to expand the $\pm\omega$ spectral component around the dc contribution as $\Gamma_{\pm}^z \approx \Gamma^z \pm \frac{\Delta}{2}\omega$. In equilibrium, detailed balance for Γ_+^z/Γ_-^z yields then $\Delta(V=0) = \frac{\Gamma_-^z}{T} \ll 1$. As we show below, despite the smallness of this correction, its relative importance is strongly enhanced in the presence of a finite dc bias V , which takes the system out of equilibrium, and may suppress the even term in the lineshape. The physical origin of Δ is in the interference of the electronic continuum in the leads with the precession of the adatom qubit at frequency ω , as is evident by the full rate calculations in Appendix B. Plugging this expansion into the generalized master equation, we find the modified steady-state polarization,

$$\langle \sigma_z^\infty \rangle = \langle \sigma_z^\infty \rangle_{\text{Bloch}} + \Delta \frac{\Omega^2 \delta\omega}{(\Gamma_\downarrow + \Gamma_\uparrow) (\tilde{\Gamma}^2 + \delta\omega^2) + \tilde{\Gamma} \Omega^2}, \quad (26)$$

which, compared to (23), has an additional contribution, *odd* in $\delta\omega$. Eq. (26), however, does not guarantee that the lineshape becomes visibly asymmetric. Defining $\Delta\sigma \equiv \langle \sigma_z^\infty \rangle - \langle \sigma_z^\infty \rangle_{\Omega=0}$, it may be written in a form compliant with Ref.⁴, Eq. (S2),

$$\Delta\sigma = \Delta\sigma_{\text{peak}} \frac{1 + 2q^* \frac{\delta\omega}{\Gamma_\Omega}}{1 + \left(\frac{\delta\omega}{\Gamma_\Omega} \right)^2}, \quad (27)$$

with $\Delta\sigma_{\text{peak}} \equiv -\frac{\Gamma_\uparrow - \Gamma_\downarrow}{\Gamma_\downarrow + \Gamma_\uparrow} \frac{\Omega^2}{\tilde{\Gamma}(\Gamma_\downarrow + \Gamma_\uparrow) + \Omega^2}$, $\Gamma_\Omega^2 \equiv \tilde{\Gamma}^2 + \frac{\tilde{\Gamma}}{\Gamma_\downarrow + \Gamma_\uparrow} \Omega^2$,

and

$$q^* = \frac{\Delta}{2} \frac{\Gamma_\downarrow + \Gamma_\uparrow}{\Gamma_\downarrow - \Gamma_\uparrow} \sqrt{1 + \frac{\Omega^2}{\tilde{\Gamma}(\Gamma_\downarrow + \Gamma_\uparrow)}}. \quad (28)$$

This so-called Fano parameter is a measure of the visibility of asymmetry in the lineshape. Note that q^* grows with Ω , in a manner consistent with Ref.⁴, Fig. (S2). Since the square root term is of the order of 1, and because $\frac{\Gamma_-^z}{T} \approx 10^{-3}$ in this experiment, visible asymmetry requires $\left| \frac{\Gamma_\downarrow - \Gamma_\uparrow}{\Gamma_\downarrow + \Gamma_\uparrow} \right| \ll 1$, or $\Gamma_\downarrow \approx \Gamma_\uparrow$. This is quite unusual that the excitation and relaxation rates are almost identical, since $T \ll \omega_d$. This points at the crucial role played by the dc voltage V , which is the most dominant energy scale in the system. Such a scenario is also consistent with the experimental observation that the measured T_1 decay time dramatically increases when this voltage is turned off³. We will now show that finite V can indeed make $\Gamma_\downarrow \approx \Gamma_\uparrow$ (and thus to make q^* significant although Δ is small), provided one also keeps in mind the distinction between the physical spin of the adatom and the effective TLS. The latter will also allow us to explain why $T_1 \gg T_2$.

The different dissipative rates can be calculated explicitly in terms of the properties of the electronic reservoirs and their couplings to the TLS. The detailed calculation is straightforward yet lengthy, and is presented in Appendix B. Under the conditions $\psi \approx \frac{\pi}{2}$, $\omega \ll T$, $\omega_d \ll V$, and full polarization of the tip, we obtain

$$\Gamma_\uparrow = \frac{\tilde{J}_s^2}{4} \alpha_\perp^2 T \left[(2\chi^2 + 1) \left(\eta_+ \left(\frac{\omega_d}{T} \right) + r \right) + 2s_{dc}\chi r \right] \quad (29a)$$

$$\Gamma_\downarrow = \frac{\tilde{J}_s^2}{4} \alpha_\perp^2 T \left[(2\chi^2 + 1) \left(\eta_- \left(\frac{\omega_d}{T} \right) + r \right) - 2s_{dc}\chi r \right] \quad (29b)$$

$$\Gamma^z = \frac{\tilde{J}_s^2}{2} \alpha_{zz}^2 T (1 + r), \quad (29c)$$

$$\Gamma_{\pm}^z = \frac{\tilde{J}_s^2}{2} \alpha_{zz}^2 [T(1 + r) \pm \omega], \quad (29d)$$

with $\eta_{\pm}(x) \equiv \pm \frac{x}{e^{\pm x} - 1}$, $\tilde{J}_s \equiv \nu_s J_s$, and $s_{dc} = \pm 1$ corresponds to the dc voltage sign. Note that we find $\Delta = \tilde{J}_s^2 \alpha_{zz}^2$. The parameters $\chi \equiv \frac{\alpha_{zx}}{\alpha_\perp}$ and $r \equiv \frac{\nu_t J_t |V|}{\nu_s J_s T}$ quantify, respectively, the projection of the adatom Hamiltonian into the effective TLS and the ratio of the atom interaction strength to the tip and the substrate. Since $\alpha_{zz} \gg \alpha_\perp$, the relaxation time T_1 becomes much longer than the dephasing time T_2 , as found in the experiment. This conclusion originates in the microscopic treatment of the system, regardless of our modification of the master equation itself. Note that although our microscopic consideration produce a ratio $\frac{\alpha_{zz}}{\alpha_\perp} \sim 4 \cdot 10^3$, experimental observation of the ratio between relaxation times suggest

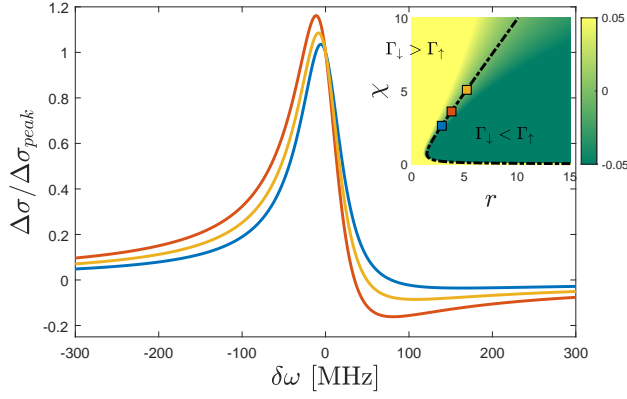


FIG. 2. Lineshapes calculated using the proposed generalized approach with $r = 2.83$, $\chi = 2.62$ (blue line), $r = 3.75$, $\chi = 3.6$ (red line), and $r = 5.2$, $\chi = 5.08$ (in yellow). Other parameters: $\Omega = 0.8$ MHz, $\Gamma^z = 6$ MHz, $\Gamma_\downarrow + \Gamma_\uparrow = 10$ KHz, $s_{dc} = 1$, $\omega_d = 25$ GHz, and $T = 12.5$ GHz $\frac{\hbar}{k_B}$. Inset: $\frac{\Gamma_\downarrow - \Gamma_\uparrow}{\Gamma_\downarrow + \Gamma_\uparrow}$ as a function of r and χ , Eq. (29a). At the dashed lines $\Gamma_\downarrow = \Gamma_\uparrow$. The colored markers correspond to the lineshapes.

that this ratio, while exceptionally large, is realistically about 1–2 orders of magnitude smaller.

Note that the value of r corresponds to the relative importance of non-equilibrium (finite bias) enhanced relaxation as compared with the thermal ones. As for χ , it is quite sensitive to the exact values of the ligand field Hamiltonian parameters in Table I, parameters that yield $\chi \approx 3$. Thus, we allow deviations from $\chi \approx 3$ so as to approach $\Gamma_\downarrow \approx \Gamma_\uparrow$. To explore these relations, in the inset to Fig. 2 the r and χ dependence of the ratio $\left| \frac{\Gamma_\downarrow - \Gamma_\uparrow}{\Gamma_\downarrow + \Gamma_\uparrow} \right|$ is plotted. It shows that small values of this ratio are plausible in a substantial regime near the black dashed line where $\Gamma_\uparrow = \Gamma_\downarrow$. Finally, let us note that not only is it required that $\Gamma_\downarrow \approx \Gamma_\uparrow$, but also that Γ_\uparrow be slightly larger than Γ_\downarrow in order to reproduce the correct lineshape, in the same orientation of the asymmetry observed in³.

We may now put everything together, and reproduce the asymmetric lineshapes using a sensible choice of the different parameters, along with staying consistent with quantities which were already measured, i.e., the rough estimates for the decay times and driving intensity that appear in³. Fig. 2 features some examples of lineshapes that have the same form as in³, with r and χ taken such that the asymmetry is visible. The parameter q^* (Eq. (28)) assumes the values 0.2–0.4 for these curves.

We note that by changing the parameters the lineshape can be flipped along either the horizontal or vertical axis. Since $\langle I_{T_0J} \rangle \propto V \alpha_{zz} \langle s_z \rangle$, changing the sign of α_{zz} due to, e.g., a change in the direction of B_z will lead to a resonant dip instead of a peak, as was observed in Refs.^{6,20}. Moreover, different microscopical parameters in the system would affect the rates $\Gamma_{\uparrow/\downarrow}$ and could change the sign of q^* , cf. Ref.⁷. A summary of the possible line shapes is given in Fig. 3 below. Notice that the plots in Fig. 2 correspond to the lower right quadrangle of Fig. 3.

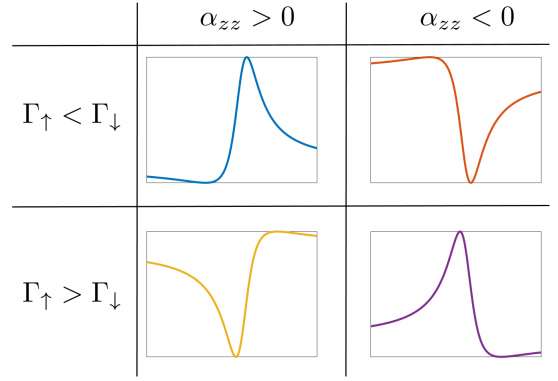


FIG. 3. Schematic line shapes given by our generalized master equation. Depending on the sign of $(\Gamma_\uparrow - \Gamma_\downarrow)$ and that of α_{zz} , the line shape can take the form of a positive or negative dip in the tunneling measurement, with an asymmetry that is “skewed” to the right or left of the resonance peak. The direct dependence of the tunneling current on the sign of V is neglected to conform with experimental conventions.

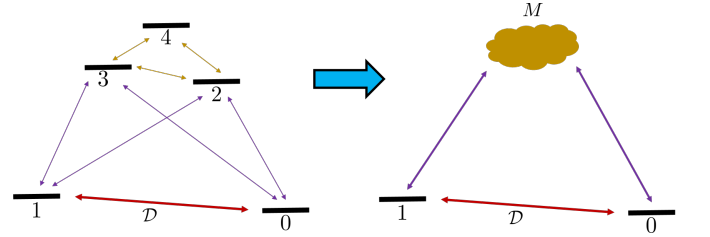


FIG. 4. Left: energy levels diagram of the Fe atom, with the different significant transition processes marked by arrows. The horizontal “coordinate” represents the $\langle S_z \rangle$ of the appropriate level. Right: the simplified diagram used in the effective master equation, exploiting the spin structure of the energy level diagram.

VI. HIGH DC VOLTAGE REGIME

A more comprehensive study of the EPR-STM properties of the system under discussion was performed in⁴. Importantly, unlike the scenario in³ we have discussed thus far, the energy scale of the bias voltage used was much higher than the energy separation between the bottom two levels of the adatom and the higher energy manifold. This makes higher adatom levels accessible, and seems to complicate our two-level treatment. However, as we will show below, the relaxation rate ratio for these levels is large, so their average population is small. This allows us to perturbatively eliminate them, while renormalizing the rate constants of the TLS.

We employ a simplified scheme, where only consider the transition rates between different energy levels (see Fig. 4), neglecting effects caused by coherences, which should decay to zero (except for the coherence of the bottom two levels, already taken into account). Next, by using the matrix elements $\langle i | S_\pm | j \rangle$ between each two

levels labeled i, j , we find the dominant transition processes. We arrive at the following conclusions:

- Each of the bottom $|0\rangle, |1\rangle$ levels is strongly connected to each of the upper $|2\rangle, |3\rangle$ levels, as seen by

$$S_{-,02} \approx S_{+,13} \approx 0.78, \quad -S_{-,03} \approx S_{+,12} \approx 0.6.$$

The magnitudes of the matrix elements with $|4\rangle$ are $\lesssim 0.08$, one order of magnitude weaker, and therefore negligible.

- The upper levels $|2\rangle, |3\rangle, |4\rangle$, are all interconnected, and the transitions $|2\rangle \leftrightarrow |4\rangle$ and $|3\rangle \leftrightarrow |4\rangle$ are of similar amplitude. We find the dominant matrix elements are $S_{-,23} \approx -0.43$, $S_{x,24} \approx 1.55$, and $iS_{y,34} \approx 1.64$.

In light of these observations, we simply approximate the upper levels as a composite state M , with new transition rates, $\Gamma_{0/1 \rightarrow M} = \Gamma_{0/1 \rightarrow 2} + \Gamma_{0/1 \rightarrow 3}$, see Fig. 4. The master equation for the occupation properties of level i , P_i , is written as

$$\frac{d}{dt}P_0 = \mathcal{D}_0 - P_0\Gamma_{0 \rightarrow M} + P_M\Gamma_{M \rightarrow 0}, \quad (30a)$$

$$\frac{d}{dt}P_1 = \mathcal{D}_1 - P_1\Gamma_{1 \rightarrow M} + P_M\Gamma_{M \rightarrow 1}, \quad (30b)$$

$$\frac{d}{dt}P_M = -P_M(\Gamma_{M \rightarrow 0} + \Gamma_{M \rightarrow 1}) + P_0\Gamma_{0 \rightarrow M} + P_1\Gamma_{1 \rightarrow M}, \quad (30c)$$

with $\mathcal{D}_0/\mathcal{D}_1$ the part coming from our novel generalized master equation for the TLS, Eqs. (20a),(20b),(25), and $\Gamma_{i \rightarrow j}$ the transition rate from level i to level j . In the steady state, $\frac{d}{dt}P_M = 0$, we find the inclusion of the M composite state results in a modification of the relaxation and excitation rates for the TLS,

$$\Gamma_{\downarrow} \rightarrow \Gamma_{\downarrow} + \frac{\Gamma_{1 \rightarrow M}\Gamma_{M \rightarrow 0}}{\Gamma_{M \rightarrow 0} + \Gamma_{M \rightarrow 1}}, \quad (31)$$

$$\Gamma_{\uparrow} \rightarrow \Gamma_{\uparrow} + \frac{\Gamma_{0 \rightarrow M}\Gamma_{M \rightarrow 1}}{\Gamma_{M \rightarrow 0} + \Gamma_{M \rightarrow 1}}. \quad (32)$$

The transition rates can then be evaluated in a similar manner to the scheme used in Appendix B. For each $\Gamma_{i \rightarrow j}$ we calculate the $\bar{\alpha}$ matrix that connects the physical spin operator to a two-level representation of levels i, j , expressed as $\vec{S} = \bar{\alpha}_{(i,j)}\vec{\sigma}$. The Pauli matrices $\vec{\sigma}$ represent the reduced Hilbert space of the two levels (i, j) . The energy difference between each two relevant levels $\Delta E_{i,j}$ is taken into account, and thermal contributions to excitation rates (i.e., ones that do not involve the bias voltage) are neglected, since $\Delta E \gg T$ when any of the higher energy levels are involved. With $\psi \approx 81^\circ$ and $V = 60$

mV, which are the parameters values in the relevant high voltage experiment⁴, we find

$$\Gamma_{M \rightarrow 0} \approx 0.73\bar{\Gamma}(1 + 6r_{ts} + r_{ts}^2), \quad \Gamma_{0 \rightarrow M} \approx 1.67\bar{\Gamma}r_{ts},$$

$$\Gamma_{M \rightarrow 1} \approx 0.73\bar{\Gamma}(1 + 4.7r_{ts} + r_{ts}^2), \quad \Gamma_{1 \rightarrow M} \approx 2.34\bar{\Gamma}r_{ts},$$

where $r_{ts} \equiv \frac{J_t \nu_t}{J_s \nu_s}$, $\bar{\Gamma} \equiv 2.15 \frac{\alpha_{\perp}^2}{4} J_s^2 \nu_s^2 \Delta E$. We observe that the ratio between the rate of exciting the adatom into the higher energy manifold, compared to the relaxation rate out of it, is of the order $r_{ts} = r \frac{T}{V}$. Since $\frac{T}{V} \sim 10^{-3}$, and we find that reproducing the experimental results dictates $r \sim 10$, our assumption of very low occupation for the high energy levels is well-justified. Crucially, we find the rates $\Gamma_{0 \rightarrow 2}$ and $\Gamma_{1 \rightarrow 3}$ are of comparable size, contradicting the existence of an appreciable spin-torque effect, where transitions between levels lowering $\langle S_z \rangle$ are favored compared to ones raising it, or vice versa, depending on the sign of the dc voltage. The comparable size of these transition rates can be traced to the fact that whereas in our earlier analysis for the $|0\rangle, |1\rangle$ levels, $\frac{\alpha_{zx}}{\alpha_{\perp}} \equiv \chi$ was an $\mathcal{O}(1)$ number (around 3), for the upper levels it is $\mathcal{O}(10^{-2})$. This, in conjunction with $\cos \psi$ being close to zero, strongly attenuates the $\langle S_z \rangle$ directionality of the inter-level transitions.

The effective TLS master equation now has, up to second order corrections in the small parameter r_{ts} ,

$$\Gamma_{\downarrow} \rightarrow \Gamma_{\downarrow} + \bar{\Gamma}(1 + \gamma), \quad (33)$$

$$\Gamma_{\uparrow} \rightarrow \Gamma_{\uparrow} + \bar{\Gamma}(1 - \gamma), \quad (34)$$

where in our calculations $\gamma \approx 0.16$. Thus, by accounting for the microscopic details of the adatom spin matrix elements, we see that both the TLS excitation and relaxation rates are increased with *comparable magnitude*. We note that reversing the bias direction will amount to taking $\gamma \rightarrow -\gamma$ in the above modification. We finally write the high voltage regime relaxation and excitation rates as

$$\begin{aligned} \Gamma_{\uparrow/\downarrow} = & \frac{\tilde{J}_s^2}{4} \alpha_{\perp}^2 T (2\chi^2 + 1) \left(\eta_{\pm} \left(\frac{\omega_d}{T} \right) + r(1 + \bar{a}) \right) \\ & \mp s_{dc} \frac{\tilde{J}_s^2}{4} \alpha_{\perp}^2 T (\bar{a}\gamma - 2\chi) r \end{aligned} \quad (35)$$

where \bar{a} is the relative amplitude of the M -assisted transitions compared to the direct ones $\bar{a} \approx \frac{2\bar{\Gamma}}{\Gamma_{\downarrow}^{ts} + \Gamma_{\uparrow}^{ts}}$, with Γ_{\downarrow}^{ts} being the tip-atom-substrate tunneling contribution. We note that by taking $\bar{a} = 0$, one recovers the rates of the low voltage regime, Eqs. (29a)–(29b). The critical line where $\Gamma_{\uparrow} = \Gamma_{\downarrow}$ depends on the voltage sign and is given by

$$r = s_{dc} \frac{\omega_d}{2T} \frac{2\chi^2 + 1}{2\chi - \bar{a}\gamma}. \quad (36)$$

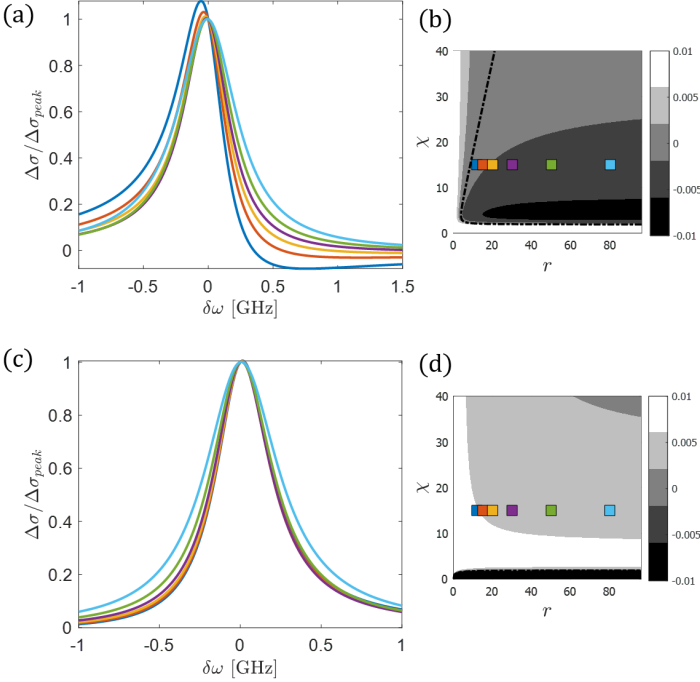


FIG. 5. (a) Lineshapes in the high voltage regime for positive bias voltage, with different values of r , representing different tip-adatom separations, for $\chi = 15$. (b) $\frac{\Gamma_{\downarrow} - \Gamma_{\uparrow}}{\Gamma_{\downarrow} + \Gamma_{\uparrow}}$ with a positive voltage, as a function of r and χ with colored markers corresponding to the different lineshapes in (a). (c), (d) are the same as (a), (b), respectively, for negative bias voltage. Other parameters (based on⁴): $\Omega = 20$ MHz, $\Gamma^z = 25$ MHz, $\Gamma_{\downarrow} + \Gamma_{\uparrow} = 0.5$ MHz, $\bar{a} = 15$, $\gamma = 0.25$, $\omega_0 = 21.5$ GHz, and $T = 25$ GHz $\frac{\hbar}{k_B}$. Case (a) corresponds to the lower right quadrangle of Fig. 3, while case (c) to the upper right one (note the renormalization by $\Delta\sigma_{peak}$ flips the lineshape sign).

To estimate the size of \bar{a} , we examine for example

$$\frac{\bar{\Gamma}}{\Gamma_{\downarrow}^{ts}} \approx \frac{\alpha_{\perp(0,2)}^2}{\alpha_{\perp(0,1)}^2} \times \frac{1}{(2\chi^2 - 2\chi + 1)2}.$$

The righthand fraction has the order of 10^{-2} , as $\chi \sim 3-8$ in our analysis thus far. However the lefthand fraction seems huge and of order 10^6 . Actually we know that $\alpha_{\perp(0,1)}^2$ is much larger than the order 10^{-3} evaluated, as discussed above in Sec. V. Taking this into account, we may estimate that $\bar{\Gamma}$ is of the same order as Γ_{\downarrow} and Γ_{\uparrow} or perhaps one order of magnitude larger, leading to an estimate of $\bar{a} \sim 10$.

The form of $\Gamma_{\uparrow/\downarrow}$ we find in Eq. (35) allows us to reproduce the main features of the experiment in Ref.⁴. As an example, the observed change in the direction of the lineshape asymmetry with reversal of the bias voltage (see Supplementary Material for Ref.⁴) is recreated in Fig. 5, with $|q^*|$ values as high as ~ 0.3 . Changing the voltage subsequently affects $\Gamma_{\uparrow}/\Gamma_{\downarrow}$, enabling a scenario where one flips the sign ($\Gamma_{\uparrow} - \Gamma_{\downarrow}$), and subsequently that of q^* , determining the asymmetry direction. Note that

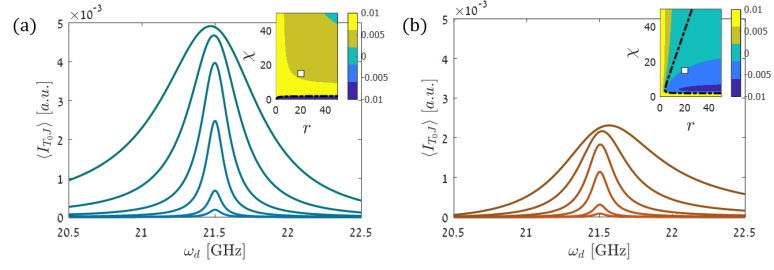


FIG. 6. Tunneling line shapes in the high voltage regime for different signs dc bias voltage [(a) positive, (b) negative], with increasing driving amplitude (bottom to top) = 1, 2, 5, 10, 20, 40 MHz. We use $\chi = 15$, $r = 20$ in both cases. Other parameters (based on the experimental results in⁴): $\Gamma^z = 25$ MHz, $\Gamma_{\downarrow} + \Gamma_{\uparrow} = 0.5$ MHz, $\bar{a} = 15$, $\gamma = 0.25$, $\omega_d = 21.5$ GHz, and $T = 25$ GHz $\frac{\hbar}{k_B}$. Insets: $\frac{\Gamma_{\downarrow} - \Gamma_{\uparrow}}{\Gamma_{\downarrow} + \Gamma_{\uparrow}}$ for different signs of the voltage, as a function of r and χ with the working point (20, 15) marked by a square.

the very different critical dashed lines in the two insets of Fig. 5 are given by Eq. (36). Moreover, the widening of the resonance with a decrease in the tip-atom separation is also apparent. This is encoded by an increase in r , which is proportional to the amplitude J_t . The decoherence rate Γ^z increases with r , naturally leading to a wider lineshape. Additionally, the reported rise in asymmetry as the driving amplitude is increased is reproduced [Eq. (28)]. This is evident in Fig. 6, where the line shapes are calculated with varying driving amplitude. One should compare this with Figs. S2 and S5B in the Supplementary Material for⁴, which clearly show similar features.

VII. CONCLUSIONS

In conclusion, we have shown that treating the adatoms in spin-polarized STM-EPR experiments as a driven open quantum system requires special care and a novel generalized approach. On the one hand, this approach should not treat the driving in a perturbative manner, such that changes in the bath spectral density as a result of small frequency shifts are resolved by the different master equation rates. On the other hand, it should be valid in the experimental parameter regime, where some of the decay rates may be significantly large compared to the driving amplitude.

We present such a treatment, which allows a clear understanding of the origin of the asymmetry in recorded lineshapes, due to the small difference in the electronic reservoirs spectral functions at 0 and $\pm\omega$. We find that even a modest difference allows for a small odd component in the lineshape [Eq. (26)], whose relative importance is greatly enhanced by the dc bias in the experiments considered.

As we have shown, completely accounting for the underlying physics of the experimental system is crucial: We find that tuning the voltage as to make the TLS re-

laxation and excitation rates close strongly suppresses the even component of the lineshape [Eq. (23)], leading to the observed asymmetry. Moreover, projecting the physical spin onto the TLS description allows one to understand the origin of the large T_1/T_2 ratio, namely the dominance of the matrix element α_{zz} , relating spin projection along the lab \hat{z} direction to the TLS polarization.

Furthermore, our novel approach enables recreating virtually all other experimental trends, even in higher voltage regimes, e.g., a change of the asymmetry sign depending on the bias voltage or on the magnetic field orientation⁴⁻⁷, and the dependence of the line shapes asymmetry on driving amplitude.

The generalized approach developed here may be useful in properly analyzing results from any future EPR-STM studies, as well as for other open quantum systems which involve non-trivial parametric regimes, e.g., hybrid quantum devices²¹⁻²³.

ACKNOWLEDGMENTS

M. G. was supported by the Israel Science Foundation (Grant No. 227/15), the German Israeli Foundation (Grant No. I-1259-303.10), the US-Israel Binational Science Foundation (Grants No. 2014262 and 2016224), and the Israel Ministry of Science and Technology (Contract No. 3-12419). B. H. acknowledges support by German-Israeli DIP project (Hybrid devices: FO 703/2-1).

Appendix A: Derivation of the generalized master equation

We derive our generalized master equation so as to solve the non-secular problem with respect to the frequencies $0, \omega$, a situation that is essential for the experimental case with $\frac{1}{T_1} < \Omega < \frac{1}{T_2}$. The starting Hamiltonian has the form (setting $\hbar = 1$)

$$H = -\frac{1}{2}\omega_0\sigma_z + \frac{\Omega}{2}(e^{i\omega_d t}\sigma_+ + e^{-i\omega_d t}\sigma_-), \\ -\frac{1}{2}(a_x\sigma_x + a_y\sigma_y + a_z\sigma_z) \otimes \hat{B} + H_B \quad (\text{A1})$$

with ω_0 the two-level energy separation, Ω the driving intensity, ω_d the driving frequency (and $\delta\omega \equiv \omega_d - \omega_0$), and H_B the bath Hamiltonian. For simplicity we will first consider the case where all the impurity operators couple to the same bath operator \hat{B} , and later on extend our results to the more general case of different bath operators. The coefficients $a_{x,y,z}$ represent some general form of coupling to the bath; we also define $a \equiv a_x + ia_y$ and $a_0 \equiv a_z$. We apply a transformation to a rotating

frame by defining $U \equiv e^{-\frac{i\omega_d t}{2}\sigma_z}$,

$$H \rightarrow UHU^\dagger + i\dot{U}U^\dagger. \quad (\text{A2})$$

Our transformed Hamiltonian reads

$$H = \frac{1}{2}\delta\omega\sigma_z + \frac{1}{2}\Omega\sigma_x \\ -\frac{1}{2}(ae^{i\omega_d t}\sigma_- + a^*e^{-i\omega_d t}\sigma_+ + a_0\sigma_z)\hat{B} + H_B. \quad (\text{A3})$$

We now diagonalize the system Hamiltonian using the transformation $\tilde{H} = S^{-1}HS$, using

$$S = \frac{1}{\sqrt{2}} \underbrace{\begin{pmatrix} \cos \frac{\beta}{2} + \sin \frac{\beta}{2} & -\cos \frac{\beta}{2} + \sin \frac{\beta}{2} \\ \cos \frac{\beta}{2} - \sin \frac{\beta}{2} & \cos \frac{\beta}{2} + \sin \frac{\beta}{2} \end{pmatrix}}_{\text{system subspace}} \otimes \mathbb{1}_{\text{bath subspace}} \quad (\text{A4})$$

with the angle β defined by $\tan \beta \equiv \frac{\delta\omega}{\Omega}$. Applying this transformation we get

$$\tilde{H} = \frac{1}{2}\omega\sigma_z - (A_0 + A_1 + A_{-1})\hat{B} + H_E, \quad (\text{A5})$$

with

$$A_0 = \left(\frac{\sin \beta}{2}a_0 + \frac{\cos \beta}{4}(a^*e^{-i\omega_d t} + ae^{i\omega_d t}) \right) \sigma_z, \quad (\text{A6a})$$

$$A_1 = \left(\frac{\sin \beta - 1}{4}a^*e^{-i\omega_d t} + \frac{\sin \beta + 1}{4}ae^{i\omega_d t} - \frac{\cos \beta}{2}a_0 \right) \sigma_-, \quad (\text{A6b})$$

$$A_{-1} = (A_1)^\dagger. \quad (\text{A6c})$$

Now that we have obtained a Hamiltonian with a diagonal system term, we move into the interaction picture, with the additional time dependence $A_k(t) \rightarrow e^{i\omega t}A_k(t)$, where $\omega = \sqrt{\Omega^2 + \delta\omega^2}$ is the generalized Rabi frequency. We may now use the Markovian expression for the time evolution of the reduced system density matrix,

$$\frac{d}{dt}\tilde{\rho}(t) = \sum_{j,k=-1}^1 \int_0^\infty ds \text{Tr}_B \left\{ \rho_B \hat{B}(s) \hat{B}(0) \right\} \times \\ \left[A_j(t-s)\tilde{\rho}(t)A_k^\dagger(t) - A_k^\dagger(t)A_j(t-s)\tilde{\rho}(t) \right] + \text{h.c.}, \quad (\text{A7})$$

with $\tilde{\rho} \equiv \frac{d+u}{2}\sigma_z + x\sigma_- + x^*\sigma_+$, the density matrix in the basis of \tilde{H} , which is different than the original (non-diagonal) “lab frame” basis. Eq. (A7), upon neglecting terms oscillating with the high frequencies $\pm\omega_d, \pm\omega_d \pm \omega, \pm 2\omega_d$ (the usual secular approximation while keeping frequencies $0, \omega, 2\omega$), leads to the master equation

$$\frac{d}{dt}\tilde{\rho}(t) = \mathcal{D}_0 + \mathcal{D}_\omega + \mathcal{D}_{2\omega} + \text{h.c.}, \quad (\text{A8})$$

with

$$\begin{aligned}
\mathcal{D}_0 \equiv & (-d\sigma_z - x^* \sigma_+) |a|^2 \left(\left(\frac{\sin \beta - 1}{4} \right)^2 \Gamma(\omega_d - \omega) + \left(\frac{\sin \beta + 1}{4} \right)^2 \Gamma(-\omega_d - \omega) \right) \\
& + (-d\sigma_z - x^* \sigma_+) \left(\frac{\cos \beta}{2} \right)^2 a_0^2 \Gamma(-\omega) \\
& + (u\sigma_z - x\sigma_-) |a|^2 \left(\left(\frac{\sin \beta + 1}{4} \right)^2 \Gamma(\omega_d + \omega) + \left(\frac{\sin \beta - 1}{4} \right)^2 \Gamma(-\omega_d + \omega) \right) \\
& + (u\sigma_z - x\sigma_-) \left(\frac{\cos \beta}{2} \right)^2 a_0^2 \Gamma(\omega) \\
& - (x\sigma_- + x^* \sigma_+) \left(\frac{\sin^2 \beta}{2} a_0^2 \Gamma(0) + |a|^2 \frac{\cos^2 \beta}{8} (\Gamma(\omega_d) + \Gamma(-\omega_d)) \right), \tag{A9a}
\end{aligned}$$

$$\begin{aligned}
D_\omega \equiv & e^{i\omega t} (-d\sigma_-) |a|^2 \cos \beta \left(\frac{\sin \beta - 1}{8} \Gamma(\omega_d - \omega) + \frac{\sin \beta + 1}{8} \Gamma(-\omega_d - \omega) \right) \\
& + e^{i\omega t} (-d\sigma_-) \frac{\cos \beta}{2} (-\sin \beta a_0^2 \Gamma(-\omega)) \\
& + e^{-i\omega t} u\sigma_+ |a|^2 \cos \beta \left(\frac{\sin \beta + 1}{8} \Gamma(\omega_d + \omega) + \frac{\sin \beta - 1}{8} \Gamma(-\omega_d + \omega) \right) \\
& + e^{-i\omega t} u\sigma_+ \frac{\cos \beta}{2} (-\sin \beta a_0^2 \Gamma(\omega)) \\
& + e^{-i\omega t} [-\sigma_+ - x\sigma_z] \frac{\cos \beta}{4} \left(\frac{\sin \beta + 1}{4} |a|^2 \Gamma(-\omega_d) + \frac{\sin \beta - 1}{4} |a|^2 \Gamma(\omega_d) - \sin \beta a_0^2 \Gamma(0) \right) \\
& + e^{i\omega t} [\sigma_- - x^* \sigma_z] \frac{\cos \beta}{4} \left(\frac{\sin \beta - 1}{4} |a|^2 \Gamma(-\omega_d) + \frac{\sin \beta + 1}{4} |a|^2 \Gamma(\omega_d) - \sin \beta a_0^2 \Gamma(0) \right), \tag{A9b}
\end{aligned}$$

$$\begin{aligned}
\mathcal{D}_{2\omega} \equiv & e^{2i\omega t} x^* \sigma_- |a|^2 \left(\frac{\sin^2 \beta - 1}{16} \Gamma(\omega_d - \omega) + \frac{\sin^2 \beta + 1}{16} \Gamma(-\omega_d - \omega) \right) \\
& + e^{2i\omega t} x^* \sigma_- \left(\frac{\cos \beta}{2} \right)^2 a_0^2 \Gamma(-\omega) \\
& + e^{-2i\omega t} x\sigma_+ |a|^2 \left(\frac{\sin^2 \beta - 1}{16} \Gamma(\omega_d + \omega) + \frac{\sin^2 \beta + 1}{16} \Gamma(-\omega_d + \omega) \right) \\
& + e^{-2i\omega t} x\sigma_+ \left(\frac{\cos \beta}{2} \right)^2 a_0^2 \Gamma(\omega), \tag{A9c}
\end{aligned}$$

and we defined the bath correlation functions

$$\Gamma(\nu) \equiv \text{Re} \left\{ \int_0^\infty d\tau e^{i\nu\tau} \text{Tr}_B \left\{ \rho_B \hat{B}(\tau) \hat{B}(0) \right\} \right\}. \tag{A10}$$

Let us note that for vanishing driving, $\Omega = 0$, one gets $\omega = \delta\omega$, $\beta = \pi/2$, hence only the spectral functions at frequencies 0 and $\pm(\omega_d + \delta\omega) = \pm\omega_0$ remain, so the dependence on ω_d disappears, as it should. The conventional secular approximation would now have allowed us to discard \mathcal{D}_ω and $\mathcal{D}_{2\omega}$ terms, but in this generalized treatment we keep these non-secular terms. In our next step, we perform a unitary transformation on the master equation (A8) with $e^{-i\tilde{H}_S t} \dots e^{i\tilde{H}_S t}$ (where $\tilde{H}_S = \frac{1}{2}\omega\sigma_z$). This introduces the coherent time evolution term $-i[\tilde{H}_S, \tilde{\rho}]$ into the righthand side of (A8),

while allowing us to eliminate the $e^{\pm i\omega t}/e^{\pm 2i\omega t}$ time dependence appearing in $\mathcal{D}_\omega/\mathcal{D}_{2\omega}$. The novel non-secular terms are now more manageable, as they do not introduce any new time dependencies into the master equation.

For the purposes of this work we may approximate $\Gamma(\pm\omega_d \pm \omega) \approx \Gamma(\pm\omega_d)$, since $\omega \ll \omega_d$, and hence deviations from this assumptions have only a minor effect on the results we present. We now define the relevant rates

$$\Gamma_\downarrow \equiv \frac{|a|^2}{2} \Gamma(\omega_d), \tag{A11a}$$

$$\Gamma_\uparrow \equiv \frac{|a|^2}{2} \Gamma(-\omega_d), \tag{A11b}$$

$$\Gamma^z \equiv \frac{a_0^2}{2} \Gamma(0), \quad (\text{A11c})$$

$$\Gamma_{\pm}^z \equiv \frac{a_0^2}{2} \Gamma(\pm\omega). \quad (\text{A11d})$$

Plugging these in, and using the inverse of (A4) to get the master equation in the original basis $\rho \equiv \frac{1}{2} + (n - \frac{1}{2})\sigma_z + \alpha^*\sigma_- + \alpha\sigma_+$, one finds that in a frame rotating with frequency ω_d (where α is transformed as $\alpha e^{-i\omega_d t} \rightarrow \alpha$), the master equation is

$$\frac{d}{dt}n = -n(\Gamma_{\downarrow} + \Gamma_{\uparrow}) + \Gamma_{\uparrow} - i\Omega \frac{\alpha - \alpha^*}{2}, \quad (\text{A12a})$$

$$\begin{aligned} \frac{d}{dt}\alpha = & -\alpha \left(\frac{\Gamma_{\downarrow} + \Gamma_{\uparrow}}{2} + (\Gamma_{+}^z + \Gamma_{-}^z) \cos^2 \beta + 2\Gamma^z \sin^2 \beta + i\delta\omega \right) \\ & -i\Omega \left(n - \frac{1}{2} \right) + \left(n - \frac{1}{2} \right) \sin \beta \cos \beta (\Gamma_{+}^z + \Gamma_{-}^z - 2\Gamma^z) \\ & - \frac{\Gamma_{+}^z - \Gamma_{-}^z}{2} \cos \beta. \end{aligned} \quad (\text{A12b})$$

By setting $\Gamma_{+}^z = \Gamma_{-}^z = \Gamma^z$ the equations reduce to the standard Bloch equations Eqs. (20a)–(20b).

Throughout our discussion it was assumed (for reasons of convenience) that the coupling was via the same bath operator \hat{B} , coupled to the system degrees of freedom via general coefficients. This need not necessarily be the case, as each $\hat{\sigma}$ operator can generally couple to a different bath operator. We could generalize the Hamiltonian used in Eq. (A1) to

$$\begin{aligned} H = & -\frac{1}{2}\hbar\omega_0\sigma_z + \frac{\Omega}{2} (e^{i\omega_d t}\sigma_+ + e^{-i\omega_d t}\sigma_-) \\ & -\frac{1}{2} (\sigma_+\hat{\Sigma}_+ + \sigma_-\hat{\Sigma}_- + \sigma_z\hat{\Sigma}_z) + H_B, \end{aligned} \quad (\text{A13})$$

Performing the prescribed diagonalization process, we get

$$\tilde{H} = \frac{1}{2}\omega\sigma_z - (A_0 + A_1 + A_{-1}) + H_B, \quad (\text{A14})$$

as before, though with the newly defined

$$A_0 = \left(\frac{\sin \beta}{2} a_z \hat{\Sigma}_z + \frac{\cos \beta}{4} (\hat{\Sigma}_- e^{-i\omega_d t} + \hat{\Sigma}_+ e^{i\omega_d t}) \right) \sigma_z, \quad (\text{A15a})$$

$$A_1 = \left(\frac{\sin \beta - 1}{4} \hat{\Sigma}_- e^{-i\omega_d t} + \frac{\sin \beta + 1}{4} \hat{\Sigma}_+ e^{i\omega_d t} - \frac{\cos \beta}{2} a_z \hat{\Sigma}_z \right) \sigma_-, \quad (\text{A15b})$$

and $A_{-1} = (A_1)^\dagger$. At first glance this seems to somewhat complicate things: whereas earlier all the correlation functions we needed to calculate were of the form $\langle \hat{B}(\tau) \hat{B}(0) \rangle$, it seems now that correlations such as $\langle \hat{\Sigma}_{\pm}(\tau) \hat{\Sigma}_z(0) \rangle$ also need to be taken into account. Luckily, this is not the case. Due to the lab frame secular approximation, where oscillations by $\pm\omega_d$ (or higher frequency) in time t are neglected, we are left only with three different bath correlation functions: $\langle \hat{\Sigma}_-(\tau) \hat{\Sigma}_+(0) \rangle$, $\langle \hat{\Sigma}_+(\tau) \hat{\Sigma}_-(0) \rangle$, and $\langle \hat{\Sigma}_z(\tau) \hat{\Sigma}_z(0) \rangle$. All other mixed products multiply terms which are negligible thanks to rapid oscillations at higher frequencies. This in turn ensures that *the structure of the generalized master equation remains unchanged*, but with more general expressions for the rates, given by

$$\Gamma_{\downarrow} \equiv \frac{1}{2} \text{Re} \left\{ \int_0^\infty d\tau e^{i\omega_d \tau} \text{Tr}_B \left\{ \rho_B \hat{\Sigma}_-(\tau) \hat{\Sigma}_+(0) \right\} \right\}, \quad (\text{A16a})$$

$$\Gamma_{\uparrow} \equiv \frac{1}{2} \text{Re} \left\{ \int_0^\infty d\tau e^{-i\omega_d \tau} \text{Tr}_B \left\{ \rho_B \hat{\Sigma}_+(\tau) \hat{\Sigma}_-(0) \right\} \right\}, \quad (\text{A16b})$$

$$\Gamma^z \equiv \frac{1}{2} \text{Re} \left\{ \int_0^\infty d\tau \text{Tr}_B \left\{ \rho_B \hat{\Sigma}_z(\tau) \hat{\Sigma}_z(0) \right\} \right\}, \quad (\text{A16c})$$

$$\Gamma_{\pm}^z \equiv \frac{1}{2} \text{Re} \left\{ \int_0^\infty d\tau e^{\pm i\omega_d \tau} \text{Tr}_B \left\{ \rho_B \hat{\Sigma}_z(\tau) \hat{\Sigma}_{\pm}(0) \right\} \right\}. \quad (\text{A16d})$$

Appendix B: Calculation of the decay rates due to tunneling electrons

In order to extract the rates that appear in the master equations (20a)–(20b), (25), it is necessary to calculate correlation functions of the reservoir electronic operators, for example,

$$\begin{aligned}
\langle \hat{\Sigma}_-(\tau) \hat{\Sigma}_+(0) \rangle &= \left(\alpha_{zx} \cos \psi + \frac{\alpha_{\perp}}{2} \sin \psi \right)^2 \sum_{k,q,\sigma} \left[\langle c_{k\sigma\ell}^\dagger(\tau) c_{k\sigma\ell}(0) \rangle \langle c_{q\sigma\ell'}(\tau) c_{q\sigma\ell'}^\dagger(0) \rangle + \ell \leftrightarrow \ell' \right] \\
&+ \left(\frac{\alpha_{\perp}}{2} (\cos \psi - 1) - \alpha_{zx} \sin \psi \right)^2 \sum_{k,q} \left[\langle c_{k\uparrow\ell}^\dagger(\tau) c_{k\uparrow\ell}(0) \rangle \langle c_{q\downarrow\ell'}(\tau) c_{q\downarrow\ell'}^\dagger(0) \rangle + \ell \leftrightarrow \ell' \right] \\
&+ \left(\frac{\alpha_{\perp}}{2} (\cos \psi + 1) - \alpha_{zx} \sin \psi \right)^2 \sum_{k,q} \left[\langle c_{k\downarrow\ell}^\dagger(\tau) c_{k\downarrow\ell}(0) \rangle \langle c_{q\uparrow\ell'}(\tau) c_{q\uparrow\ell'}^\dagger(0) \rangle + \ell \leftrightarrow \ell' \right]. \quad (\text{B1})
\end{aligned}$$

Let us illustrate the calculation of the last product of correlation functions appearing in the above expression, defining

$$C(\tau) \equiv \sum_{k,q} \langle c_{q\downarrow\ell'}^\dagger(\tau) c_{q\downarrow\ell'}(0) \rangle \langle c_{k\uparrow\ell}(\tau) c_{k\uparrow\ell}^\dagger(0) \rangle. \quad (\text{B2})$$

Each of these correlations can be expressed in terms of the Fermi-Dirac distribution,

$$\langle c_{q\downarrow\ell'}^\dagger(\tau) c_{q\downarrow\ell'}(0) \rangle = f_{\ell',\downarrow}(\epsilon_q) e^{i\epsilon_q\tau}, \quad (\text{B3})$$

$$\langle c_{k\uparrow\ell}(\tau) c_{k\uparrow\ell}^\dagger(0) \rangle = [1 - f_{\ell,\uparrow}(\epsilon_k)] e^{-i\epsilon_k\tau}, \quad (\text{B4})$$

with the subscripts of f indicating the lead and spin direction. Allowing an additional finite voltage V between the leads (may be set to zero for inter-lead tunneling), we find

$$\begin{aligned}
C(\tau) &= \sum_{k,q} f_{\ell',\downarrow}(\epsilon_q) [1 - f_{\ell,\uparrow}(\epsilon_k)] e^{-i(\epsilon_k - \epsilon_q + V)\tau} \\
&\approx \nu_{\ell'\downarrow} \nu_{\ell\uparrow} \int d\epsilon' \int d\epsilon f(\epsilon') [1 - f(\epsilon)] e^{-i(\epsilon - \epsilon' + V)\tau}, \quad (\text{B5})
\end{aligned}$$

where $\nu_{\ell'\downarrow}$ represents the density of states for \downarrow -electrons in lead ℓ' , and $\nu_{\ell\uparrow}$ the density of states for \uparrow -electrons in

lead ℓ . The densities of states are approximated to be roughly constant near the Fermi energy.

Next, we Laplace transform this correlation function in order to retrieve its spectral features. Since we only use the real part of the bath correlation functions in our analysis (as they represent the rates governing the master equation; the imaginary parts correspond to shifts of the subsystem Hamiltonian, whose effect we have verified to be small), we exploit the relation between the Fourier and Laplace transforms $\mathcal{F}\{C\} = 2\text{Re}\{\mathcal{L}\{C\}\}$ (due to the property $C(-\tau) = C^*(\tau)$) and calculate the Fourier transform instead,

$$\begin{aligned}
C(\omega) &\equiv \int_{-\infty}^{\infty} d\tau e^{i\omega\tau} C(\tau) \\
&= \nu_{l\downarrow} \nu_{r\uparrow} \int d\epsilon f(\epsilon) [1 - f(\epsilon + \omega - V)]. \quad (\text{B6})
\end{aligned}$$

Let us now define

$$\begin{aligned}
I_{\pm}(\omega, V) &\equiv \int d\epsilon f(\epsilon) [1 - f(\epsilon + \omega \pm V)] \\
&= T\eta_{\pm}(\omega \pm V), \quad (\text{B7})
\end{aligned}$$

with $\eta_{\pm}(x) \equiv \pm \frac{x}{e^{\pm x} - 1}$. We arrive at the full expressions for the spectral functions,

$$\begin{aligned}
\langle \hat{\Sigma}_- \hat{\Sigma}_+ \rangle(\omega) &= \left(\alpha_{zx} \cos \psi + \frac{\alpha_{\perp}}{2} \sin \psi \right)^2 (\nu_{\ell\uparrow} \nu_{\ell'\uparrow} + \nu_{\ell\downarrow} \nu_{\ell'\downarrow}) (I_-(\omega, V) + I_+(\omega, V)) \\
&+ \left(\frac{\alpha_{\perp}}{2} (\cos \psi - 1) - \alpha_{zx} \sin \psi \right)^2 (\nu_{\ell\uparrow} \nu_{\ell'\downarrow} I_-(\omega, V) + \nu_{\ell\downarrow} \nu_{\ell'\uparrow} I_+(\omega, V)) \\
&+ \left(\frac{\alpha_{\perp}}{2} (\cos \psi + 1) - \alpha_{zx} \sin \psi \right)^2 (\nu_{\ell\uparrow} \nu_{\ell'\downarrow} I_+(\omega, V) + \nu_{\ell\downarrow} \nu_{\ell'\uparrow} I_-(\omega, V)), \quad (\text{B8a})
\end{aligned}$$

$$\begin{aligned}
\langle \hat{\Sigma}_+ \hat{\Sigma}_- \rangle(\omega) &= \left(\alpha_{zx} \cos \psi + \frac{\alpha_{\perp}}{2} \sin \psi \right)^2 (\nu_{\ell\uparrow} \nu_{\ell'\uparrow} + \nu_{\ell\downarrow} \nu_{\ell'\downarrow}) (I_-(\omega, V) + I_+(\omega, V)) \\
&+ \left(\frac{\alpha_{\perp}}{2} (\cos \psi - 1) - \alpha_{zx} \sin \psi \right)^2 (\nu_{\ell\uparrow} \nu_{\ell'\downarrow} I_+(\omega, V) + \nu_{\ell\downarrow} \nu_{\ell'\uparrow} I_-(\omega, V)) \\
&+ \left(\frac{\alpha_{\perp}}{2} (\cos \psi + 1) - \alpha_{zx} \sin \psi \right)^2 (\nu_{\ell\uparrow} \nu_{\ell'\downarrow} I_-(\omega, V) + \nu_{\ell\downarrow} \nu_{\ell'\uparrow} I_+(\omega, V)), \quad (\text{B8b})
\end{aligned}$$

$$\begin{aligned} \langle \hat{\Sigma}_z \hat{\Sigma}_z \rangle (\omega) = & \left(\alpha_{zz} \cos \psi + \frac{\alpha_{xz}}{2} \sin \psi \right)^2 (\nu_{\ell\uparrow} \nu_{\ell'\uparrow} + \nu_{\ell\downarrow} \nu_{\ell'\downarrow}) (I_- (\omega, V) + I_+ (\omega, V)) \\ & + \left(\frac{\alpha_{xz}}{2} \cos \psi - \alpha_{zz} \sin \psi \right)^2 (\nu_{\ell\uparrow} \nu_{\ell'\downarrow} + \nu_{\ell\downarrow} \nu_{\ell'\uparrow}) (I_- (\omega, V) + I_+ (\omega, V)). \end{aligned} \quad (\text{B8c})$$

We may now calculate the contributions of different tunneling processes to the master equation rates: tip-atom-substrate tunneling $[(\ell, \ell') = (t, s)]$, tip-atom-tip tunneling $[(\ell, \ell') = (t, t)]$, and substrate-atom-substrate tunneling $[(\ell, \ell') = (s, s)]$. This is done by using the densities of state

$$\nu_{t\sigma} = \frac{\nu_t}{2} (1 + \sigma p), \quad \nu_{s\uparrow} = \nu_{s\downarrow} = \frac{\nu_s}{2}, \quad (\text{B9})$$

with $p \in [0, 1]$ determining the level of polarization in the tip. Collecting the different terms together with the proper coupling constants for each process, we find

$$\begin{aligned} \Gamma_{\downarrow} = & \frac{1}{2} (J_s^2 \nu_s^2 + J_t^2 \nu_t^2) \frac{\omega_d}{1 - e^{-\beta \omega_d}} \left(\alpha_{zx}^2 + \frac{\alpha_{\perp}^2}{2} \right) \\ & + J_t^2 \frac{\nu_t^2}{2} \frac{\omega_d}{1 - e^{-\beta \omega_d}} p^2 \left[\left(\alpha_{zx}^2 - \frac{\alpha_{xx}^2}{4} \right) \cos 2\psi - \frac{\alpha_{\perp}^2}{4} + \alpha_{zx} \alpha_{\perp} \sin 2\psi \right] \\ & + J_s J_t \frac{\nu_s \nu_t}{2} \frac{V + \omega_d}{1 - e^{-\beta(V + \omega_d)}} \left[\alpha_{zx}^2 + \frac{\alpha_{\perp}^2}{2} - p \alpha_{\perp} \left(\alpha_{zx} \sin \psi - \frac{\alpha_{\perp}}{2} \cos \psi \right) \right], \end{aligned} \quad (\text{B10})$$

$$\begin{aligned} \Gamma_{\uparrow} = & \frac{1}{2} (J_s^2 \nu_s^2 + J_t^2 \nu_t^2) \frac{\omega_d}{e^{\beta \omega_d} - 1} \left(\alpha_{zx}^2 + \frac{\alpha_{\perp}^2}{2} \right) \\ & + J_t^2 \frac{\nu_t^2}{2} \frac{\omega_d}{e^{\beta \omega_d} - 1} p^2 \left[\left(\alpha_{zx}^2 - \frac{\alpha_{xx}^2}{4} \right) \cos 2\psi - \frac{\alpha_{\perp}^2}{4} + \alpha_{zx} \alpha_{\perp} \sin 2\psi \right] \\ & + J_s J_t \frac{\nu_s \nu_t}{2} \frac{V - \omega_d}{1 - e^{-\beta(V - \omega_d)}} \left[\alpha_{zx}^2 + \frac{\alpha_{\perp}^2}{2} + p \alpha_{\perp} \left(\alpha_{zx} \sin \psi - \frac{\alpha_{\perp}}{2} \cos \psi \right) \right], \end{aligned} \quad (\text{B11})$$

$$\begin{aligned} \Gamma^z = & J_s^2 \frac{\nu_s^2}{2} T \left(\alpha_{zz}^2 + \frac{\alpha_{xz}^2}{4} \right) \\ & + J_t^2 \frac{\nu_t^2}{2} T \left[\alpha_{zz}^2 (1 + p^2 \cos 2\psi) + \frac{\alpha_{xz}^2}{4} (1 - p^2 \cos 2\psi) + p^2 \alpha_{zz} \alpha_{xz} \sin 2\psi \right] \\ & + J_s J_t V \frac{\nu_s \nu_t}{2} \left(\alpha_{zz}^2 + \frac{\alpha_{xz}^2}{4} \right), \end{aligned} \quad (\text{B12})$$

$$\begin{aligned} \Gamma_{\pm}^z = & J_s^2 \frac{\nu_s^2}{2} T \left(1 \pm \frac{\omega}{T} \right) \left(\alpha_{zz}^2 + \frac{\alpha_{xz}^2}{4} \right) \\ & + J_t^2 \frac{\nu_t^2}{2} T \left(1 \pm \frac{\omega}{T} \right) \left[\alpha_{zz}^2 (1 + p^2 \cos 2\psi) + \frac{\alpha_{xz}^2}{4} (1 - p^2 \cos 2\psi) + p^2 \alpha_{zz} \alpha_{xz} \sin 2\psi \right] \\ & + J_s J_t V \frac{\nu_s \nu_t}{2} \left(\alpha_{zz}^2 + \frac{\alpha_{xz}^2}{4} \right), \end{aligned} \quad (\text{B13})$$

where we used the fact that $V \gg T, \omega_d, \omega$ and $\omega \ll T$, to make some simplifications. We now employ some additional approximations, compliant with the experimental setup:

1. $\alpha_{zz} \gg \alpha_{xz}$, since according to Eq. (7) there is a four-orders-of-magnitude difference between them.
2. $p \approx 1$ – taking the polarization level to be maximal

allows us to simplify the above expressions greatly, without modifying the underlying physics in any meaningful way, as we have explicitly checked.

3. $\psi \approx \frac{\pi}{2}$ – in accordance with the experiments^{3,4}.

After defining $\tilde{J}_s \equiv J_s \nu_s$, $\tilde{J}_t \equiv J_t \nu_t$, $\tilde{J}_t \equiv r \tilde{J}_s \frac{T}{V}$ and

$\alpha_{zx} \equiv \chi\alpha_{\perp}$, we may finally write

$$\Gamma_{\downarrow} \approx \frac{\tilde{J}_s^2}{4} \alpha_{\perp}^2 \left(2\chi^2 + 1 + r^2 \frac{T^2}{V^2} \right) \frac{\omega_d}{1 - e^{-\beta\omega_d}} + \frac{\tilde{J}_s^2}{4} \alpha_{\perp}^2 (2\chi^2 - 2\chi + 1) \frac{rT \left(1 + \frac{\omega_d}{V} \right)}{1 - e^{-\beta(V+\omega_d)}}, \quad (\text{B14})$$

$$\Gamma_{\uparrow} \approx \frac{\tilde{J}_s^2}{4} \alpha_{\perp}^2 \left(2\chi^2 + 1 + r^2 \frac{T^2}{V^2} \right) \frac{\omega_d}{e^{\beta\omega_d} - 1} + \frac{\tilde{J}_s^2}{4} \alpha_{\perp}^2 (2\chi^2 + 2\chi + 1) \frac{rT \left(1 - \frac{\omega_d}{V} \right)}{1 - e^{-\beta(V-\omega_d)}}, \quad (\text{B15})$$

$$\Gamma^z \approx \frac{\tilde{J}_s^2 T}{2} (1 + r) \alpha_{zz}^2, \quad (\text{B16})$$

$$\Gamma_{\pm}^z \approx \Gamma^z \pm \frac{\tilde{J}_s^2}{2} \alpha_{zz}^2 \omega. \quad (\text{B17})$$

Neglecting terms such as $\frac{\omega_d}{V} \approx 0.02$ and $\frac{T}{V} \approx 0.01$ due to the overwhelming size of the voltage energy scale yields the expressions that we use in the main text, Eqs. (29a)–(29c). Note that we assume that r is an order $\mathcal{O}(1)$ parameter, implying $\tilde{J}_s \gg \tilde{J}_t$, which is physically sensible since the adatom is much closer to the substrate than to the tip.

-
- ¹ A. Abragam and B. Bleaney, *Electron paramagnetic resonance of transition ions*, International series of monographs on physics (Clarendon P., 1970).
- ² S. Loth, M. Etzkorn, C. P. Lutz, D. M. Eigler, and A. J. Heinrich, *Science* **329**, 1628 (2010).
- ³ S. Baumann, W. Paul, T. Choi, C. P. Lutz, A. Ardavan, and A. J. Heinrich, *Science* **350**, 417 (2015).
- ⁴ P. Willke, W. Paul, F. D. Natterer, K. Yang, Y. Bae, T. Choi, J. Fernández-Rossier, A. J. Heinrich, and C. P. Lutz, *Science Advances* **4** (2018), 10.1126/sciadv.aag1543.
- ⁵ T. Choi, C. P. Lutz, and A. J. Heinrich, *Current Applied Physics* **17**, 1513 (2017).
- ⁶ T. Choi, W. Paul, S. Rolf-Pissarczyk, A. J. Macdonald, F. D. Natterer, K. Yang, P. Willke, C. P. Lutz, and A. J. Heinrich, *Nature Nanotechnology* **12**, 420 EP (2017).
- ⁷ P. Willke, Y. Bae, K. Yang, J. L. Lado, A. Ferrón, T. Choi, A. Ardavan, J. Fernández-Rossier, A. J. Heinrich, and C. P. Lutz, *Science* **362**, 336 (2018), <http://science.sciencemag.org/content/362/6412/336.full.pdf>.
- ⁸ S. Müllegger, S. Tebi, A. K. Das, W. Schöffberger, F. Faschinger, and R. Koch, *Phys. Rev. Lett.* **113**, 133001 (2014).
- ⁹ Y. Manassen, M. Averbukh, M. Jbara, B. Siebenhofer, A. Shnirman, and B. Horovitz, *Journal of Magnetic Resonance* **289**, 107 (2018).
- ¹⁰ F. I. Dalidchik, E. M. Balashov, and S. A. Kovalevskiy, *JETP Letters* **105**, 314 (2017).
- ¹¹ S. Baumann, F. Donati, S. Stepanow, S. Rusponi, W. Paul, S. Gangopadhyay, I. G. Rau, G. E. Pacchioni, L. Gragnaniello, M. Pivetta, J. Dreiser, C. Piamonteze, C. P. Lutz, R. M. Macfarlane, B. A. Jones, P. Gambardella, A. J. Heinrich, and H. Brune, *Phys. Rev. Lett.* **115**, 237202 (2015).
- ¹² J. Fransson, O. Eriksson, and A. V. Balatsky, *Phys. Rev. B* **81**, 115454 (2010).
- ¹³ B. Mollow and M. Miller, *Annals of Physics*, **52**, 464 (1969).
- ¹⁴ R. E. Slusher and H. M. Gibbs, *Phys. Rev. A* **5**, 1634 (1972).
- ¹⁵ R. Dum, A. S. Parkins, P. Zoller, and C. W. Gardiner, *Phys. Rev. A* **46**, 4382 (1992).
- ¹⁶ K. Yang, Y. Bae, W. Paul, F. D. Natterer, P. Willke, J. L. Lado, A. Ferrón, T. Choi, J. Fernández-Rossier, A. J. Heinrich, and C. P. Lutz, *Phys. Rev. Lett.* **119**, 227206 (2017).
- ¹⁷ G. Lindblad, *Comm. Math. Phys.* **48**, 119 (1976).
- ¹⁸ V. Gorini, A. Kossakowski, and E. Sudarshan, *Journal of Mathematical Physics* **17**, 821 (1975).
- ¹⁹ A. Redfield, in *Advances in Magnetic Resonance*, Advances in Magnetic and Optical Resonance, Vol. 1, edited by J. S. Waugh (Academic Press, 1965) pp. 1 – 32.
- ²⁰ T. Choi, C. P. Lutz, and A. J. Heinrich, *Current Applied Physics* **17**, 1513 (2017).
- ²¹ G. Kurizki, P. Bertet, Y. Kubo, K. Māžlmer, D. Petrosyan, P. Rabl, and J. Schmiedmayer, *Proceedings of the National Academy of Sciences* **112**, 3866 (2015).
- ²² E. Togan, Y. Chu, A. S. Trifonov, L. Jiang, J. Maze, L. Childress, M. V. Dutt, A. S. Sorensen, P. Hemmer, A. S. Zibrov, and M. Lukin, in *Frontiers in Optics 2011/Laser Science XXVII* (Optical Society of America, 2011) p. FThL4.
- ²³ J. Morton and B. Lovett, *Annual Review of Condensed Matter Physics* **2**, 189 (2011).